

## Article

# Study on Structure and Properties of La<sub>2</sub>O<sub>3</sub>-Doped Basaltic Glasses for Immobilizing Simulated Lanthanides

Qin Tong<sup>1,2,3</sup> , Jichuan Huo<sup>1,4,\*</sup>, Xingquan Zhang<sup>1,3,\*</sup>, Zhu Cui<sup>5</sup> and Yongchang Zhu<sup>3,5</sup>

<sup>1</sup> State Key Laboratory of Environment-Friendly Energy Materials, Southwest University of Science and Technology, Mianyang 621010, China; tongqin518@163.com

<sup>2</sup> Electromechanic Engineering College, Mianyang Teachers' College, Mianyang 621000, China

<sup>3</sup> Fundamental Science on Nuclear Wastes and Environmental Safety Laboratory, Southwest University of Science and Technology, Mianyang 621010, China; zyc\_qy@163.com

<sup>4</sup> Analysis and Testing Center, Southwest University of Science and Technology, Mianyang 621010, China

<sup>5</sup> Ceramics Science Institute, China Building Materials Academy, Beijing 100024, China; 13520204133@139.com

\* Correspondence: huojichuan@swust.edu.cn (J.H.); zhangxingquan@swust.edu.cn (X.Z.); Tel./Fax: +86-816-6089506 (J.H.)

**Abstract:** The La<sub>2</sub>O<sub>3</sub>-doped basaltic glass simulated high-level waste form (HLW) was prepared by the solid-state melt method. The simulated waste La<sub>2</sub>O<sub>3</sub> maximum loading and the doping effect on structure, thermal stability, leaching behavior, density, and hardness of basaltic glasses were studied. XRD and SEM results show that the simulated waste loading of La<sub>2</sub>O<sub>3</sub> in basaltic glass can be up to ~46 wt.%, and apatite (CaLa<sub>4</sub>(SiO<sub>4</sub>)<sub>3</sub>O) precipitates when the content of La<sub>2</sub>O<sub>3</sub> reaches 56 wt.%. Raman results indicate that the addition of La<sub>2</sub>O<sub>3</sub> breaks the Si–O–Si bond of large-membered and four-membered, but the number of Al<sup>3+</sup> involved in the formation of the network increase. Low content of La<sub>2</sub>O<sub>3</sub> can help to repair the glass network, but it destroys the network as above 26 wt.%. DSC results show the thermal stability of simulated waste forms first increases and then decreases with the increase of La<sub>2</sub>O<sub>3</sub> content. With the increase of La<sub>2</sub>O<sub>3</sub> content, the density of the simulated waste form increases, and the hardness decreases. The leaching chemical stability of samples was evaluated by the ASTM Product Consistency Test (PCT) Method, which show that all the samples have good chemical stability. The leaching rates of La and Fe are three orders of magnitude lower than those of the other elements. Among them, L36 has the best comprehensive leaching performance.

**Keywords:** La<sub>2</sub>O<sub>3</sub>-doped; basaltic glass; HLW; PCT



**Citation:** Tong, Q.; Huo, J.; Zhang, X.; Cui, Z.; Zhu, Y. Study on Structure and Properties of La<sub>2</sub>O<sub>3</sub>-Doped Basaltic Glasses for Immobilizing Simulated Lanthanides. *Materials* **2021**, *14*, 4709. <https://doi.org/10.3390/ma14164709>

Academic Editor: Carlo Maria Carbonaro

Received: 19 July 2021

Accepted: 18 August 2021

Published: 20 August 2021

**Publisher's Note:** MDPI stays neutral with regard to jurisdictional claims in published maps and institutional affiliations.



**Copyright:** © 2021 by the authors. Licensee MDPI, Basel, Switzerland. This article is an open access article distributed under the terms and conditions of the Creative Commons Attribution (CC BY) license (<https://creativecommons.org/licenses/by/4.0/>).

## 1. Introduction

The disposal of high-level nuclear wastes (HLW) coming from the reprocessing of spent nuclear fuel is still an international problem, which is characterized by strong radioactivity, long half-life and tremendous harm. Vitrification has been considered to be one of the most effective methods for immobilization radioactive wastes, especially HLW, and it is the only industrialized curing technology in the world [1–3]. High Level Liquid Waste (HLLW) from the reprocessing of spent fuel is rich in dozens of elements [4–6], among which lanthanides make up a significant proportion. Lanthanide elements with special electron shell structure have great influence on the structure and properties of glass [7,8]. Therefore, as a typical representative of lanthanide elements, it is of great significance to study the effect of lanthanum content on the structure and properties of glass.

Basalt has existed for more than 100 million years in nature with holocrystalline texture, hypocrySTALLINE texture and glassy texture, which has stable chemical and physical properties and strong weathering resistance [9]. Through the high temperature melting in nature, basalt has a good ability to form glass network [10]. Natural basaltic rocks contain a small amount of radioactive elements (such as uranium and thorium), which have been stable for billions of years. Therefore, the glass and glass-ceramics waste forms

prepared with natural basaltic rocks can be considered as a suitable waste form for HLW immobilization. Immobilizing HLW with basaltic glass-ceramics was studied in the United States last century, which is used to deal with HLW and transuranic waste from commercial and military production, including nuclear waste from the Idaho Chemical Plant and the Savannah Plant and zeolite used to purify reactor core waste from the Three Mile Island accident [4]. Therefore, basalt is expected to be a new generation of host materials for HLW.

At present, there have been some researches on  $\text{La}_2\text{O}_3$ -doped basaltic glasses in the world. Feng et al. proved La, Al, and Na are exclusively bonded to  $\text{PO}_4$  groups and no bond was formed between these positive ions by NMR [11]. Bin et al. studied the structure of lanthanum-iron phosphate glasses by Raman and found a small amount of  $\text{La}_2\text{O}_3$  couldn't change the structure of the glass network and  $\text{La}^{3+}$  can enhance the stability of glass structures [12]. Sheng et al. found the degree of polymerization of glass first increases and then decreases with the increase of doping content of  $\text{La}_2\text{O}_3$  [13]. Based on the existing literature, it can be considered that the content of  $\text{La}_2\text{O}_3$  has a great influence on the structure and properties of glass [14–16]. But the study of  $\text{La}_2\text{O}_3$ -doped basaltic glasses is rare. So, through some research in this paper, it hopes to make some contributions to the long and in-depth study on basaltic glasses as host materials for HLW.

## 2. Experimental Method

### 2.1. Fabrication of Simulated Waste Glass

The components of the basaltic glass (Sichuan Aerospace Tuoxin Basalt Industrial CO., Ltd., Chengdu, China) were listed in Table 1. The designed samples were labeled as LX ( $X = 0, 8, 16, 26, 36, 46, 56$ ) based on the mass ratio of  $\text{La}_2\text{O}_3$  (MACKLIN, 99.99%) (0%, 8%, 16%, 26%, 36%, 46%, and 56%, respectively). The raw materials were mixed by ball-milling (QM-3SP2, Planetary ball mill, Nanjing NanDa Instrument Plant, Nanjing, China) for 30 min. About 30 g of the mixtures were heated in a corundum crucible in air at 1450 °C for 3 h to form homogeneous melts and then annealed at 600 °C for 1 h, followed by cooling to room temperature.

**Table 1.** Components of the basaltic glass from producer.

Raw Materials	Chemical Components, wt. %								
	$\text{SiO}_2$	$\text{Al}_2\text{O}_3$	$\text{Fe}_2\text{O}_3$	$\text{CaO}$	$\text{MgO}$	$\text{TiO}_2$	$\text{Na}_2\text{O}$	$\text{K}_2\text{O}$	$\text{La}_2\text{O}_3$
L0	54.97	14.24	7.38	15.63	2.80	2.29	1.24	0.77	-
L8	50.57	13.10	6.79	14.38	2.58	2.11	1.14	0.71	8
L16	46.17	11.96	6.20	13.13	2.35	1.92	1.04	0.65	16
L26	40.68	10.54	5.46	11.57	2.07	1.69	0.92	0.57	26
L36	35.18	9.11	4.72	10.00	1.79	1.47	0.79	0.49	36
L46	29.68	7.69	3.99	8.44	1.51	1.24	0.67	0.42	46
L56	24.19	6.27	3.25	6.88	1.23	1.01	0.55	0.34	56

### 2.2. Characterization

X-ray diffraction (XRD, PANalytical Company, Eindhoven, The Netherlands) data was collected on an X' Pert PRO diffractometer using  $\text{Cu-K}\alpha$  radiation ( $\lambda = 1.54187 \text{ \AA}$ ). The microstructure and microtopography of the samples were studied using a Carl Zeiss Ultra 55 field emission scanning electron microscope (FE-SEM) with energy dispersive X-ray spectroscopy (EDS), and the flat block samples were corroded with 10% HF and sprayed with gold. Raman spectra was collected to characterize the vibration of the characteristic functional group of the samples using laser Raman spectrometer with CCD detector (InVia, Renishaw, UK). Spectra were acquired in the 200–2000  $\text{cm}^{-1}$  range. The glass powders of particle size less than 200 mesh were measured using differential scanning calorimetry (DSC SDT Q600, TA Instruments Inc., New Castle, DE, USA) to determine glass transition temperature ( $T_g$ ), the crystallization peak temperature  $T_p$  and incipient crystallization temperatures ( $T_c$ ) from room temperature to room temperature–1300 °C at a rate of 10 °C/min in air. Bulk densities of the samples were determined using Archimedes

method. Vickers hardness of the samples were measured using microhardness tester (TMVS-1S, Auto-instrument CO., Ltd., Kejing, Shenyang, China) with loading 100 g and charging for 10 s.

### 2.3. Chemical Stability

The leaching chemical stability of the obtained samples was evaluated by the ASTM Product Consistency Test (PCT) Method [17]. The powder samples sieved between 100 and 200 meshes cleaned with deionized water and dried. Then 1.5 g of sample was soaked in 15 mL deionized water in Teflon reactors and kept in an oven at  $90 \pm 2$  °C. Leachates were taken from the reactors at the end of 1, 3, 7, 14, 28 days respectively, and then 15 mL new deionized water was added. The ion concentrations (Si, Ca, Al, Fe, La) in leachate were obtained by inductively coupled plasma mass spectrometry (ICP-MS, 7700X, Agilent Technologies, Santa Clara, CA, USA). The normalized elemental leaching rate  $LR_i$  ( $\text{g}\cdot\text{m}^{-2}\cdot\text{d}^{-1}$ ) can be expressed by the following Equation (1):

$$LR_i = \frac{C_i}{f_i \left( \frac{S}{V} \right) t} \quad (1)$$

where  $C_i$  is the concentration of the  $i$ -th element in solution ( $\text{g}\cdot\text{L}^{-1}$ ),  $f_i$  is the mass fraction of the  $i$ -th element in the sample,  $V$  is the volume of the solution (L),  $S$  is the powered samples surface area ( $\text{m}^2$ ),  $t$  refers to the soaking time (d).

## 3. Results and Discussion

### 3.1. Glass and Crystallization Behavior

Figure 1 illustrates XRD patterns of the L0-L56. When  $L = 0-46$  in LX, it is glassy, however, all of the diffraction peaks are consistent with apatite ( $\text{CaLa}_4(\text{SiO}_4)_3\text{O}$ ; PDF#71-1368) with L56. It indicates that the loading of  $\text{La}_2\text{O}_3$  in basaltic glass is up to 46 wt.%.

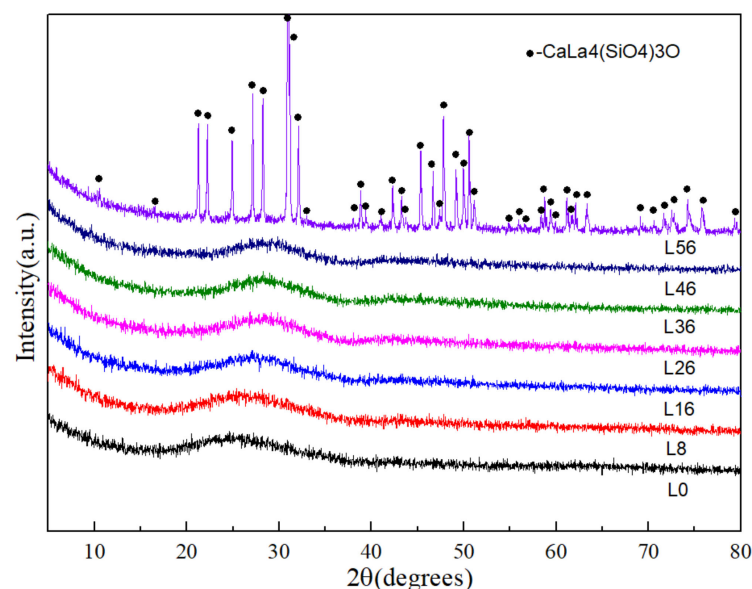
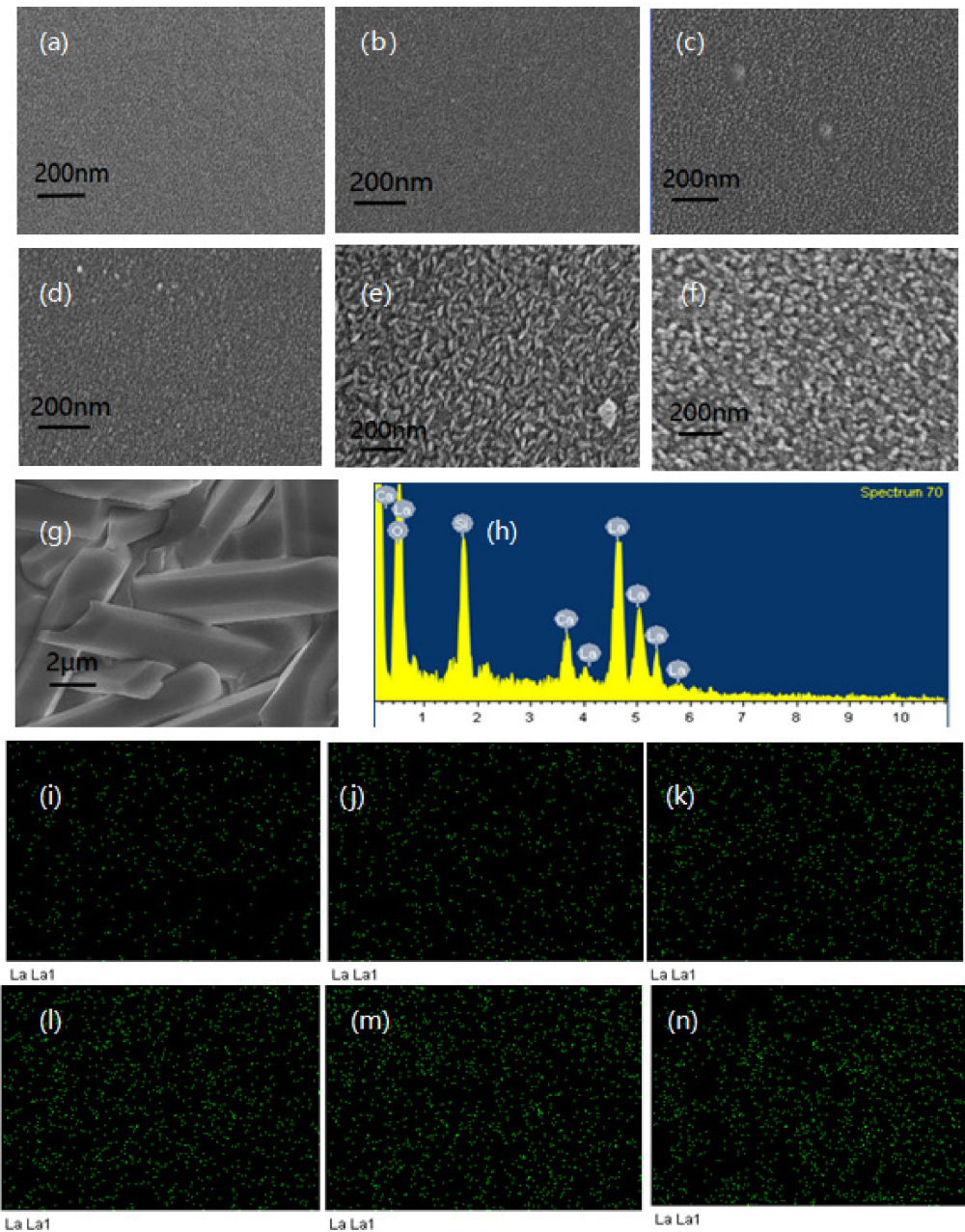


Figure 1. XRD patterns from L0 to L56.

### 3.2. SEM and EDX Analysis

Figure 2 shows SEM images of the basaltic glasses L0-L56 (a-g), elemental mapping of La from L8-L56 (h-m) and EDX spectra under the (g) image region (n). Figure 2a-f shows the crack shape of the glasses become more and more obvious with the increase of  $\text{La}_2\text{O}_3$  content, which may be attributed to the effect of  $\text{La}_2\text{O}_3$  on the glass structure. And, it is also obvious that there are no crystals in the basaltic glasses L0-L46, which is

consistent with the XRD results. Figure 2g shows the rod-shaped crystals with a hexagonal cross section were found in the sample of L56. According to the EDX spectra as shown in Figure 2h, the precipitated crystalline phases should be consistent with the results of phase analysis. It shows that the distribution of La is basically uniform from Figure 2i–n, indicating La solidifies well in basaltic glass.



**Figure 2.** (a–g) SEM image of L0–L56. (h) EDX spectra under the (g) image region. (i–n) Elemental mapping of La from L8–L56.

### 3.3. Raman Analysis

In order to explore how the shape of Raman spectra varies with glass composition, we compared selected representative spectra from samples covering the entire compositional range (Figure 3). The Raman spectra of basaltic glasses can be divided into three bands: the low wavenumber (LW) band ( $400\text{--}650\text{ cm}^{-1}$ ), the middle wavenumber (MW) band ( $650\text{--}850\text{ cm}^{-1}$ ), and the high wavenumber (HW) band ( $850\text{--}1200\text{ cm}^{-1}$ ).

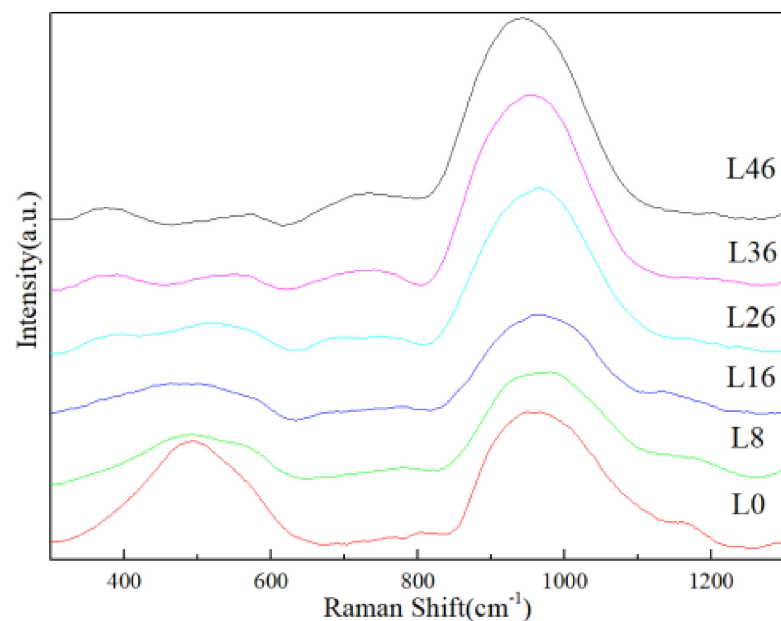


Figure 3. Raman spectra of basaltic glasses from L0 to L46.

The LW band is attributed to low energy bending vibrations of bridging oxygens in a T–O–T configuration, or to angular deformation of  $\text{TO}_4$  groups in a O–T–O configuration, where T = Si, Al and Fe, in tetrahedral rings [18–22]. The characteristic peaks located at 442, 492, and 604  $\text{cm}^{-1}$  are attributed to mixed stretching–bending vibrational modes of Si–O–Si in large-membered ( $\geq 5$ ), four-membered, and three membered rings, respectively [23]. Figure 3 shows that the peak of L0 in the low wavenumber is mainly located at 500  $\text{cm}^{-1}$ , indicating the main role of Si–O–Si vibration of the four-membered ring. With the increase of  $\text{La}_2\text{O}_3$  content, the peak gradually recedes and changes to two peaks at 400  $\text{cm}^{-1}$  and 600  $\text{cm}^{-1}$ , indicating the addition of  $\text{La}_2\text{O}_3$  breaks the Si–O–Si bond of large-membered and four-membered. The peak at 400  $\text{cm}^{-1}$  and 600  $\text{cm}^{-1}$  should be related to Al and Fe [18,20].

The Raman peak at the MW band (650–850  $\text{cm}^{-1}$ ) is ascribed to symmetrical stretching vibration of Al–NBO (non-bridging oxygen) [20,23]. The enhancement of peak intensity indicates that the number of  $\text{Al}^{3+}$  involved in the formation of the network increase.

The HW band (850–1200  $\text{cm}^{-1}$ ) is attributed to the vibrations of T–O $^-$  bonds—where O $^-$  stands for BO (bridging oxygen) or NBO [24]. The more bridge oxygens T is connected to, the higher wave number of T–O $^-$  vibration moves to, otherwise, the fewer oxygens it's connected to [25]. Figure 3 shows the peak moves slightly towards the high wave number from L0–L26, when the content of  $\text{La}_2\text{O}_3$  exceeds 26 wt.% (L26–L46), the peak position moves slightly to the low wave number, but it doesn't change much. This is also indirectly stated although  $\text{La}_2\text{O}_3$  breaks the Si–O–Si bond,  $\text{Al}^{3+}$  is more involved in the network connection. Meanwhile, the slight shift of the peak indicates that the glass network is repaired first with the addition of  $\text{La}_2\text{O}_3$  content, and the glass network is destroyed when the content of  $\text{La}_2\text{O}_3$  exceeds 26 wt.%. This may be attributed to the fact that although the addition of  $\text{La}_2\text{O}_3$  breaks the Si–O–Si bond, when the  $\text{La}_2\text{O}_3$  content is low, La with high field intensity can enter the gap of the glass network and link the anion groups as charge compensation to repair the glass network. When the content of  $\text{La}_2\text{O}_3$  is too high, the NBO in the glass network increases significantly because of too much free oxygen provided by  $\text{La}_2\text{O}_3$ , which destroys the glass network [12,15,26,27].

### 3.4. DSC Curves

In the process of long-term deep geological disposal, the temperature of solidified waste forms will rise due to the large amounts of heat released by the decay of radioactive elements. Therefore, solidified waste forms require good thermal stability [4,28,29]. LAFI et al. proposed to use  $(T_c - T_g)$  to character the thermal stability of glass [30]. They proved

that the greater the  $(T_c - T_g)$  value, the less likely the glass is to nucleate and crystallize, and the better the thermal stability of the glass. Saad and Poulin used parameter  $S$  to represent the thermal stability of glass [31]. The greater the value of thermal stability parameter  $S$  by the following Equation (2), the better the thermal stability of glass.

$$S = (T_p - T_c) (T_p - T_g) / T_g \quad (2)$$

where  $S$  is thermal stability parameter,  $T_p$  is the crystallization peak temperature (K),  $T_c$  is incipient crystallization temperatures (K),  $T_g$  is glass transition temperature (K).

Figure 4 shows DSC curve of basaltic glasses from L0 to L56. Table 2 lists the glass transition temperature  $T_g$ , the initial temperature of the first crystallization peak  $T_c$ , the crystallization peak temperature  $T_p$  and the thermal stability parameter  $S$  of L0–L46. Figure 4 illustrates the glass transition temperature of the simulated waste forms increases and the crystallization peak splits from one to two with the increase of  $\text{La}_2\text{O}_3$  content. It is speculated that the second crystallization peak may be related to apatite, which means there may be apatite crystals in L16–L46 that are too small to detect. The  $T_g$  increases with the increase of  $\text{La}_2\text{O}_3$  content except L56, which may be related to the crystallization of L56. Table 2 indicates the thermal stability of glass-cured body firstly increases with the increase of  $\text{La}_2\text{O}_3$  content, and then decreases when the content of  $\text{La}_2\text{O}_3$  exceeds 8 wt.%, which may be related to changes in the glass structure. According to the previous analysis, the addition of a small amount of  $\text{La}_2\text{O}_3$  is conducive to repairing the glass network, increasing the level of network connectivity and thus improving the thermal stability. However, excessive  $\text{La}_2\text{O}_3$  will lead to the increase of “non-bridging oxygen” in the system which decreases the level of network connectivity and reduces the thermal stability of glass [32].

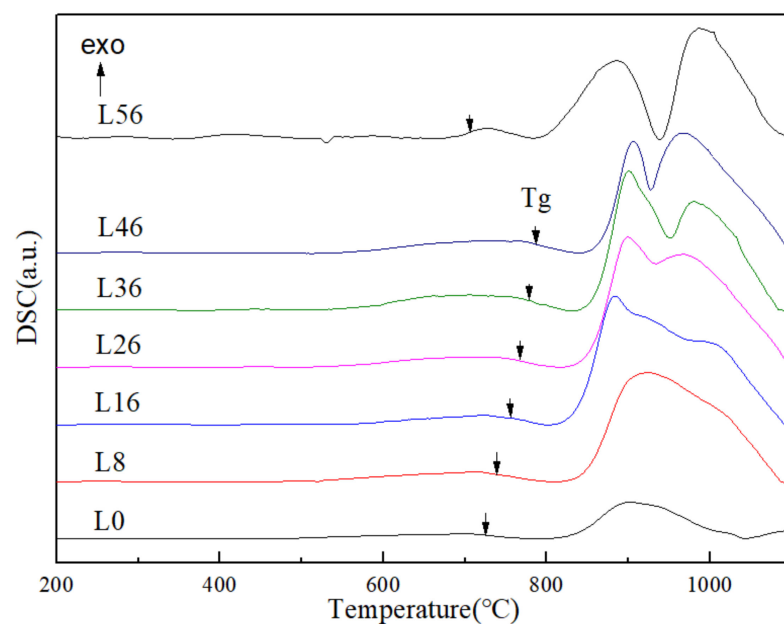


Figure 4. DSC curve of basaltic glasses from L0 to L56.

Table 2. The obtained  $T_g$ ,  $T_c$ ,  $T_p$  and  $S$  of L0–L46.

Sample	L0	L8	L16	L26	L36	L46
$T_g$ (°C)	725.836	738.402	745.46	766.88	778.716	787.449
$T_c$ (°C)	803.836	819.402	811.46	823.88	835.716	843.449
$T_p$ (°C)	901.803	922.402	884.46	898.88	899.716	905.449
$S$	17.26	18.74	9.96	9.52	7.36	6.90

### 3.5. Density and Hardness

Table 3 shows the densities and hardness of basaltic glasses. It indicates that the densities increase and the hardness decreases with the increase of  $\text{La}_2\text{O}_3$  content. As  $\text{La}^{3+}$  is located in the gap of glass network as modifier and has a higher coordination number (8 coordination), the glass network structure is more compact with the increase of  $\text{La}_2\text{O}_3$  content, which shows an increase in the density of glasses macroscopically [12,33]. However,  $\text{La}_2\text{O}_3$  cannot participate in the formation of the network [34]. The more  $\text{La}_2\text{O}_3$  is added, the less network former exists, resulting in the loose structure of the glass network framework, which is macroscopically manifested as decreased hardness of the glass.

**Table 3.** Density and Vickers hardness of L0–L46.

Sample	L0	L8	L16	L26	L36	L46
Density ( $\text{g}/\text{cm}^3$ )	2.5025	2.7504	2.9856	3.2029	3.3918	3.5034
Vickers hardness	898.52	825.80	775.84	716.42	623.04	521.20

### 3.6. Leaching Characteristics

The chemical stability of the samples ( $X = 0\text{--}46$  in LX) were evaluated by Product Consistency Test (PCT) Method. The computed results of the normalized leaching rates of Si, Ca, Al, Fe and La are depicted in Figure 5. It shows that the leaching rate of most samples decreased significantly with the increase of leaching time in the first 7 days, and the decreasing rate slowed down after 7 days, and basically remained unchanged after 14 days. which may be attributed to the “gel layer” hinder the leaching behavior formed by the re-polymerization of Si in solution at the interface layer of vitreous reaction with solution [35,36]. The  $LR_{\text{La}}$  and  $LR_{\text{Fe}}$  are three orders of magnitude lower than those of the other elements. After 28 d immersion, the leaching rate of each element is as low as  $LR_{\text{Si}} = 5.38 \times 10^{-4} \text{ g}\cdot\text{m}^{-2}\cdot\text{d}^{-1}$  (L36),  $LR_{\text{Ca}} = 1.38 \times 10^{-3} \text{ g}\cdot\text{m}^{-2}\cdot\text{d}^{-1}$  (L36),  $LR_{\text{Al}} = 1.49 \times 10^{-3} \text{ g}\cdot\text{m}^{-2}\cdot\text{d}^{-1}$  (L16),  $LR_{\text{Fe}} = 1.3 \times 10^{-6} \text{ g}\cdot\text{m}^{-2}\cdot\text{d}^{-1}$  (L26),  $LR_{\text{La}} = 5.82 \times 10^{-7} \text{ g}\cdot\text{m}^{-2}\cdot\text{d}^{-1}$  (L26), respectively. It can be concluded from Figure 5a–e that L36 has the best comprehensive leaching performance, which leaching rates of Al, Fe, and La are  $LR_{\text{Al}} = 1.96 \times 10^{-3} \text{ g}\cdot\text{m}^{-2}\cdot\text{d}^{-1}$ ,  $LR_{\text{Fe}} = 2.82 \times 10^{-6} \text{ g}\cdot\text{m}^{-2}\cdot\text{d}^{-1}$ ,  $LR_{\text{La}} = 8.22 \times 10^{-7} \text{ g}\cdot\text{m}^{-2}\cdot\text{d}^{-1}$ , respectively. Figure 5b shows the  $LR_{\text{Ca}}$  of L26 and L46 is higher than that of other samples. Figure 5e shows the  $LR_{\text{La}}$  decreases with the increase of La content in the simulated waste forms, but it increases as above 36 wt.%. This may be attributed to the effect of La on glass structure. The leaching rates of all the samples meet the expectations of nuclear industry standards ( $<1 \text{ g}\cdot\text{m}^{-2}\cdot\text{d}^{-1}$ ) [37], indicating that L0–L46 has good chemical stability.

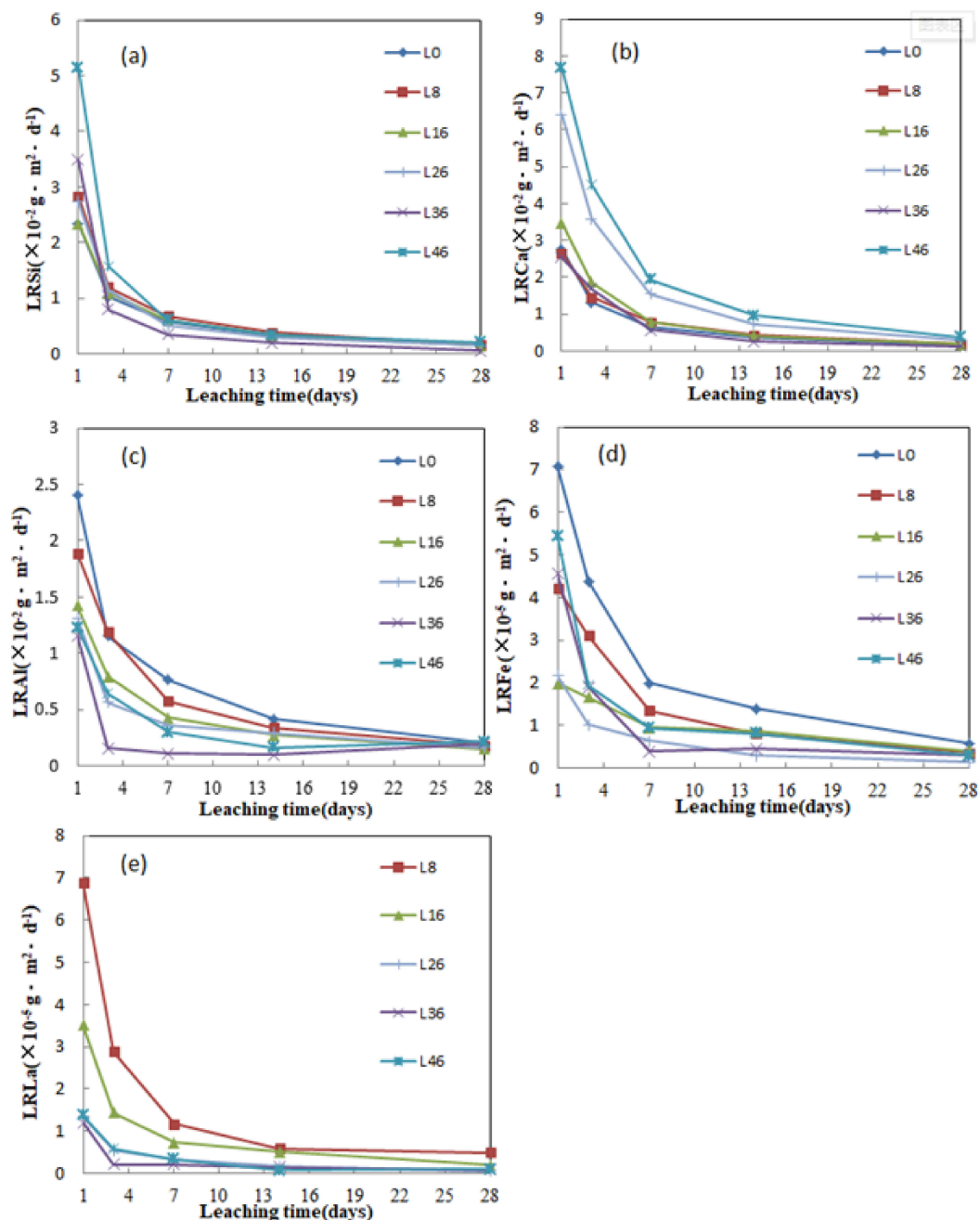


Figure 5. Normalized elemental leach rates of (a) Si, (b) Ca, (c) Al, (d) Fe, and (e) La of the L0–L46.

#### 4. Conclusions

The  $\text{La}_2\text{O}_3$ -doped basaltic glass simulated waste forms were prepared by the solid-state melt method. The loading of  $\text{La}_2\text{O}_3$  in the simulated waste forms is at least 46 wt.%, and apatite ( $\text{CaLa}_4(\text{SiO}_4)_3\text{O}$ ) is precipitated from the glass when the content of  $\text{La}_2\text{O}_3$  reaches 56 wt.%. The addition of  $\text{La}_2\text{O}_3$  breaks the Si–O–Si bond of large-membered and four-membered, but the number of  $\text{Al}^{3+}$  involved in the formation of the network is increasing. When  $\text{La}_2\text{O}_3$  loading is low, it can help to repair the glass network with the increase of  $\text{La}_2\text{O}_3$  content, but it destroys the network when above 26 wt.%. With the increase of  $\text{La}_2\text{O}_3$  content, the densities of basaltic glasses increase and the hardness decreases, which may be related to the effect of adding  $\text{La}_2\text{O}_3$  on glass structure and the reduction of network former. The addition of a small amount of  $\text{La}_2\text{O}_3$  is beneficial to improve the thermal stability of the glass, but excessive  $\text{La}_2\text{O}_3$  reduces the thermal stability

of the glass. The simulated waste forms have good chemical stability, and L36 has the best comprehensive leaching performance. The  $LR_{La}$  and  $LR_{Fe}$  are three orders of magnitude lower than those of the other elements.

**Author Contributions:** Conceptualization, J.H. and Y.Z.; methodology, X.Z. and Z.C.; validation, J.H.; investigation, Q.T.; resources, J.H.; data curation, Q.T.; writing—original draft preparation, Q.T.; writing—review and editing, J.H. and X.Z.; supervision, J.H.; project administration, J.H. All authors have read and agreed to the published version of the manuscript.

**Funding:** This research was supported by the Longshan academic talent research supporting program of Southwest University of Science and Technology, China, grant numbers 18LZX560 and 18LZXT10; major Science and Technology Special Project of Advanced Materials in Sichuan Province, China, grant number 2019ZDZX0023 and national defense key discipline laboratory of nuclear waste and environmental safety, China, grant number 17kfhk03.

**Institutional Review Board Statement:** Not Applicable.

**Informed Consent Statement:** Not Applicable.

**Data Availability Statement:** The data can be requested from the corresponding author.

**Conflicts of Interest:** The authors declare no conflict of interest.

## References

1. Wang, Y.; Wang, F.; Wang, Q.; Zhu, H.; Xiang, G.; Liao, Q.; Zhu, Y. Effect of neodymium on the glass formation, dissolution rate and crystallization kinetic of borophosphate glasses containing iron. *J. Non-Cryst. Solids* **2019**, *526*, 119726. [[CrossRef](#)]
2. Gin, S.; Abdelouas, A.; Criscenti, L.; Ebert, W.; Ferrand, K.; Geisler, T.; Harrison, M.; Inagaki, Y.; Mitsui, S.; Mueller, K.; et al. An international initiative on long-term behavior of high-level nuclear waste glass. *Mater. Today* **2013**, *16*, 243–248. [[CrossRef](#)]
3. Day, D.E.; Wu, Z.; Ray, C.S.; Hrma, P. Chemically durable iron phosphate glass waste forms. *J. Non-Cryst. Solids* **1998**, *241*, 1–12. [[CrossRef](#)]
4. Donald, I.W.; Metcalfe, B.L.; Taylor, R.N.J. The immobilization of high level radioactive wastes using ceramics and glasses. *J. Mater. Sci.* **1997**, *32*, 5851–5887. [[CrossRef](#)]
5. He, Y.; Lu, Y.; Zhang, Q. Characterization of monazite glass–ceramics as wasteform for simulated  $\alpha$ -HLLW. *J. Nucl. Mater.* **2008**, *376*, 201–206. [[CrossRef](#)]
6. Ojovan, M.I.; Lee, W.E. *An Introduction to Nuclear Waste Immobilisation*; Elsevier: Amsterdam, The Netherlands, 2005.
7. Wang, M.; Fang, L.; Li, M.; Cheng, J.; He, F.; Deng, W.; Dongol, R. Dependence of  $Gd_2O_3$  containing silicate glass workability and fragility on structure. *Mater. Chem. Phys.* **2016**, *179*, 304–309. [[CrossRef](#)]
8. Xiao, L.; Xiao, Q.; Liu, Y.; Ai, P.; Li, Y.; Wang, H. A transparent surface-crystallized  $Eu^{2+}$ ,  $Dy^{3+}$  co-doped strontium aluminate long-lasting phosphorescent glass-ceramic. *J. Alloy. Compd.* **2010**, *495*, 72–75. [[CrossRef](#)]
9. Lai, S.C. *Petrology of Magmatic Rocks*, 2nd ed.; Higher Education Press: Beijing, China, 2016.
10. Liu, J.; Cui, Y.; Yang, J.; Wu, Z.; Amp, N. Effect of basalt composition and mineral on high temperature melting process. *J. Yanshan Univ.* **2017**, *41*, 323–328.
11. Shi, F.; Hu, L.; Cui, Y.; Ren, J. Revealing the Structures in Short- and Middle-Order of Lanthanum-Doped  $Al_2O_3$ – $NaPO_3$  Glasses by Solid State NMR Spectroscopy. *J. Phys. Chem. C* **2021**, *125*, 2097–2110. [[CrossRef](#)]
12. Qian, B.; Liang, X.; Yang, S.; Gao, L.; Guo, X. Raman spectra study on the structure of lanthanum-iron phosphate glasses. *Chin. J. Inorg. Chem.* **2013**, *29*, 314–318.
13. Li, S.; Lu, Y.; Qu, Y.; Kang, J.; Yue, Y.; Liang, X. Dielectric and thermal properties of aluminoborosilicate glasses doped with mixed rare-earth oxides. *J. Non-Cryst. Solids* **2020**, *556*, 120550. [[CrossRef](#)]
14. Lu, Y.; Liu, H.; Qu, Y.; Lu, H.; Huang, S.; Yue, Y. Influence of  $La_2O_3$  and  $Ce_2O_3$  additions on structure and properties of aluminoborosilicate glasses. *J. Mater. Sci. Mater. Electron.* **2016**, *28*, 2716–2722. [[CrossRef](#)]
15. Wang, M.; Fang, L.; Li, M.; Liu, Z.; Yan, Y.; Zhang, X. Effect of rare earth dopant on thermal stability and structure of  $ZnO$ – $B_2O_3$ – $SiO_2$  glass. *J. Inorg. Mater.* **2017**, *32*, 643–648.
16. Xu, K.; Yan, Y.; Zhang, L.; Pan, H.; Zhao, J.; Jia, X.; Wang, G.; Wu, H. Study on structural, dielectric, thermal and chemical characteristics of aluminoborosilicate glasses doped by rare earth oxides. *Mater. Technol.* **2014**, *29*, A40–A43. [[CrossRef](#)]
17. ASTM C1285-14. *Standard Test Methods for Determining Chemical Durability of Nuclear, Hazardous, and Mixed Waste Glasses and Multiphase Glass Ceramics: The Product Consistency Test (PCT)*; ASTM International: West Conshohocken, PA, USA, 2014.
18. Ahmadzadeh, M.; Scrimshire, A.; Mottram, L.; Stennett, M.C.; Hyatt, N.C.; Bingham, P.A.; McCloy, J.S. Structure of  $NaFeSiO_4$ ,  $NaFeSi_2O_6$ , and  $NaFeSi_3O_8$  glasses and glass-ceramics. *Am. Miner.* **2020**, *105*, 1375–1384. [[CrossRef](#)]
19. Kline, J.; Tangstad, M.; Tranell, G. Raman spectroscopic study of the structural modifications associated with the addition of calcium oxide and boron oxide to silica. *Metall. Mater. Trans. B* **2015**, *46B*, 62–73. [[CrossRef](#)]

20. Lu, P.; Xia, W.; Jiang, H.; Zhao, H. Analysis of high alumina silicate glass with infrared and raman spectroscopy. *Bull. Chin. Ceram. Soc.* **2015**, *34*, 878–887.
21. Iguchi, Y.; Kashio, S.; Goto, T.; Nishina, Y.; Fuwa, T. Raman spectroscopic study on the structure of silicate slags. *Can. Metall. Q.* **1981**, *20*, 51–56. [[CrossRef](#)]
22. Zheng, K.; Liao, J.; Wang, X.; Zhang, Z. Raman spectroscopic study of the structural properties of CaO-MgO-SiO<sub>2</sub>-TiO<sub>2</sub> slags. *J. Non-Cryst. Solids* **2013**, *376*, 209–215. [[CrossRef](#)]
23. Bechgaard, T.K.; Mauro, J.; Bauchy, M.; Yue, Y.; Lamberson, L.A.; Jensen, L.R.; Smedskjaer, M.M. Fragility and configurational heat capacity of calcium aluminosilicate glass-forming liquids. *J. Non-Cryst. Solids* **2017**, *461*, 24–34. [[CrossRef](#)]
24. Tarrago, M.; Royo, I.; Martínez, S.; Garcia-Valles, M.; Neuville, D.R. Incorporation of calcium in glasses: A key to understand the vitrification of sewage sludge. *Int. J. Appl. Glas. Sci.* **2021**, *12*, 367–380. [[CrossRef](#)]
25. Cui, J.; Cao, X.; Wang, P.; Shi, L.; Zhong, S.; Zhao, F.; Gao, Q.; Li, J. Infrared and raman spectroscopy analysis of substrate glass and cover glass in liquid crystal display. *Bull. Chin. Ceram. Soc.* **2020**, *39*, 3664–3668.
26. Abo-Mosallam, H.; Park, H. Crystallization characteristics of La<sub>2</sub>O<sub>3</sub>-containing glasses for glass ionomer cement. *Mater. Lett.* **2012**, *72*, 137–140. [[CrossRef](#)]
27. Luo, Z.; Lu, A.; Han, L. Effects of doping La<sub>2</sub>O<sub>3</sub> on crystallization and mechanical properties of lithium disilicate glass—Ceramics. *Chin. J. Nonferrous Met.* **2009**, *19*, 2018–2023.
28. Bingham, P.; Hand, R.; Forder, S. Doping of iron phosphate glasses with Al<sub>2</sub>O<sub>3</sub>, SiO<sub>2</sub> or B<sub>2</sub>O<sub>3</sub> for improved thermal stability. *Mater. Res. Bull.* **2006**, *41*, 1622–1630. [[CrossRef](#)]
29. Li, X.; Tao, X.; Xiao, Z.; Kong, L.; Liu, Y.; Zeng, X.; Yang, K.; Shi, J. Structure and properties of iron phosphate wasteforms loaded with simulated radioactive waste enriched in SrO and alkali metal oxides. *J. Ceram.* **2020**, *41*, 904–912.
30. Lafi, O.A.; Imran, M.M.A. Compositional dependence of thermal stability, glass-forming ability and fragility index in some Se–Te–Sn glasses. *J. Alloy. Compd.* **2011**, *509*, 5090–5094. [[CrossRef](#)]
31. Saad, M.; Poulain, M. Glass forming ability criteria. *Mater. Sci. Forum* **1987**, *19*, 11–18. [[CrossRef](#)]
32. Novatski, A.; Steimacher, A.; Medina, A.N.; Bento, A.C.; Baesso, M.L.; Andrade, L.H.; Lima, S.M.; Guyot, Y.; Boulon, G. Relations among nonbridging oxygen, optical properties, optical basicity, and color center formation in CaO–MgO aluminosilicate glasses. *J. Appl. Phys.* **2008**, *104*, 094910. [[CrossRef](#)]
33. Kang, U.; Zhilin, A.; Logvinov, D.P.; Onushchenko, A.A.; Savost'yanov, V.A.; Chuvaeva, T.I.; Shashkin, A.V. Transparent Nd<sup>3+</sup>-Activated Glass-Ceramics in the Li<sub>2</sub>O–Al<sub>2</sub>O<sub>3</sub>–SiO<sub>2</sub> System: Physicochemical Aspects of Their Preparation and Optical Characteristics. *Glas. Phys. Chem.* **2001**, *27*, 344–352. [[CrossRef](#)]
34. Lu, P.; Zheng, Y.; Cheng, J.; Guo, D. Effect of La<sub>2</sub>O<sub>3</sub> addition on crystallization and properties of Li<sub>2</sub>O–Al<sub>2</sub>O<sub>3</sub>–SiO<sub>2</sub> glass-ceramics. *Ceram. Int.* **2013**, *39*, 8207–8212. [[CrossRef](#)]
35. Geisler, T.; Janssen, A.; Scheiter, D.; Stephan, T.; Berndt, J.; Putnis, A. Aqueous corrosion of borosilicate glass under acidic conditions a new corrosion mechanism. *J. Non-Cryst. Solids* **2010**, *356*, 1458–1465. [[CrossRef](#)]
36. Ma, T.; Liang, W.; Xu, H.; Li, W.; Zhao, J.; Han, X. Research progress on dissolution behavior and mechanisms of radioactive waste glasses. *J. Nucl. Radiochem.* **2019**, *41*, 411–417.
37. EJ 1186-2005. *Characterization of Radioactive Waste Forms and Packages*; Nuclear Industry Standard in China, Commission for Science, Technology and Industry for National Defense: Beijing, China, 2005.